An alternative synthesis of magnetic biochar from green coconut husks and its application for simultaneous and individual removal of caffeine and salicylic acid from aqueous solution

Bruno Salarini Peixoto[a,c], Larissa Silva de Oliveira Mota[a], Isac Marinho Dias[a], Beatrice Muzzi[b], Martin Albino[b,c], Michele Petrecca[b,c], Claudia Innocenti[c], Pamella Christina Ortega de Oliveira[a], Gilberto Alves Romeiro[a], Claudio Sangregorio[b,c], Marcela Cristina de Moraes[a,*], mcmoraes@id.uff.br

[a]Chemistry Institute, Fluminense Federal University - Outeiro de São João Batista, Niterói, RJ 24020-141, Brazil

[b]Institute of Chemistry of Organometallic Compounds, C.N.R., 50019 Sesto Fiorentino, FI, Italy

[c]Department of Chemistry 'Ugo Schiff' & INSTM, University of Florence, 50019 Sesto Fiorentino, FI, Italy

*Corresponding author.

Editor: ~~<>~~Xin Yang

~~ABSTRACT~~Abstract

Efficient remediation of water pollutants requires the continuous development of new technologies. Magnetic biochars offer a sustainable solution by combining the high adsorptive capacity of biochar with easy adsorbent recovery. However, the main existing methods for synthesizing magnetic carbons have some disadvantages, such as obtaining materials with a poor magnetic response or with less surface area available for the adsorption of contaminants. Thus, there is an evident need to develop new methods for the synthesis of magnetic carbons. This study presents an innovative approach to obtaining a magnetic nanocomposite **(MNC)**. Initially, chemically activated biochar **(ACP)** was produced from the pyrolysis of green coconut husks **(GCH)**. Subsequently, an oleic acid-coated magnetite colloid was employed to incorporate magnetic nanoparticles into the porous structure of **ACP**. Two additional magnetic carbons were prepared using co-pyrolysis of **GCH** or **GCH** biochar, both impregnated with $FeCl_3$ solution, for performance comparison. Characterization of **MNC** revealed a high BET surface area ~~(1019 m~~(1019 $m^2 \cdot g^{~~-1~~-1}$) and favorable magnetism ~~(11.2 ± 1.1~~(11.2 ± 1.1 $emu \cdot g^{~~-1~~-1}$). The **MNC** exhibited similar or superior adsorption capacities for caffeine ~~(153~~(153 $mg \cdot g^{~~-1~~-1}$) and salicylic acid ~~(203~~(203 $mg \cdot g^{~~-1~~-1}$) when compared to the other materials. These findings highlight the ability of this innovative process to provide a material with good magnetic properties and concomitantly high surface area, resulting in a promising adsorbent for the removal of contaminants from water.

Keywords:

Activated carbon, Adsorption, Biochar, Biomass, Caffeine, Magnetic biochar, Magnetic nanocomposite, Salicylic acid

Data ~~availability~~Availability

Data will be made available on request.

1 Introduction

Several organic compounds, including pharmaceuticals and pesticides, have been found in the effluents of several cities due to incorrect disposal and the inefficiency of the conventional wastewater treatment (WWT) processes in their removal. Disposing of these substances in water bodies directly impacts aquatic life and the human population, which will inevitably ingest these contaminants through water and food consumption [1,2].

Among the different physicochemical processes that can be used to remove emerging contaminants in water, the process of adsorption with activated carbon stands out due to its ease of application, efficiency, and relatively low cost [3–8]. Moreover, there is increasing evidence indicating that biochar plays a significant role in influencing microbial metabolism in several energy and environmental applications, including soil and water remediation [9–12]. Given its ability to mediate microbial degradation of contaminants and its inherent adsorbent properties, biochar emerges as a highly promising option for biological water treatment.

Among the main difficulties associated with using activated carbons as adsorbents in water treatment plants is the high operating cost of separating the fine particulate from the effluent, and for this reason, granular activated carbon is used instead of powder, with larger particles and lower surface area. The filtration of large volumes of water requires large amounts of energy, discouraging the use of materials that could result in further pressure drops. One of the ways to overcome this disadvantage is to combine activated carbon with magnetic particles, generating a magnetic composite material easily recoverable by different magnetic separation methods, such as applying an external electromagnetic field or using permanent magnets [7,13–15].

The main methods for synthesizing magnetic carbons comprise 1) the co-precipitation of iron oxide (magnetite) on the surface of a biochar or porous carbon material; and 2) the pyrolysis of lignocellulosic or carbonaceous material, impregnated with iron salt [16]. However, these processes have some disadvantages. Synthesis by coprecipitation results in a great decrease in the available surface area. Furthermore, unattached magnetic particles are removed from reaction medium along with the obtained composite, disturbing the properties of the material [15]. When following the methodology of biomass pyrolysis with iron salts, controlling the biochar porosity is arduous. It is also difficult controlling the size and crystallinity of the particles, which can result in materials with a poor magnetic response [13,14].

Therefore, the need to develop alternative methodologies capable of providing magnetic-activated carbons with adequate magnetic properties and high adsorptive capacity becomes evident. This article presents a novel method for obtaining magnetic activated carbon/biochar with enhanced control over its properties through the parallel synthesis of biochar and magnetic particles, followed by their subsequent combination. In this method, magnetic nanoparticles, in the form of oleic acid-coated magnetite

colloid, were incorporated into the porous structure of activated carbon derived from green coconut husks. The product is compared with activated carbons obtained from different methodologies for removing emerging contaminants in water, using salicylic acid and caffeine as model contaminants.

2 Methodology

2.1 Materials preparation

The pericarp (husks) of green coconuts (*Cocos nucifera* L.) discarded by bars and restaurants in the city of Rio de Janeiro (22°37'49″ S, 55°09'37″ W) was used to prepare the materials. The fruits were washed with water and cut, manually removing the edible pulp residues, then oven-dried (105 °C) and ground.

2.2 Preparation of magnetic biochars

The first methodology consisted of mixing the dried mass of milled green coconut husks with an aqueous solution of iron (III) chloride ($FeCl_3$) in a ~~1:1 weight~~ 1:1 wt ratio (biomass / $FeCl_3$~~·6H~~·6 H_2O). After one hour of stirring, the water was removed using a rotary evaporator followed by drying the material in an oven at ~~105 °C.~~ 105 °C. This material was then inserted into the pyrolysis system and heated at ~~500 °C~~ 500 °C for ~~90~~90 min using a continuous flow of ~~500~~500 mL·min~~$^{-1}$~~$^{-1}$ of nitrogen gas. After pyrolysis, the solid obtained was washed with ultrapure water and magnetically separated using a permanent magnet. The produced material was named **MBC1** [17].

The second methodology employed for magnetic biochar preparation was similar to the previous one, replacing crushed coconut with coconut biochar**.** Initially, the coconut biochar (**BC**) was obtained through the slow pyrolysis of the green coconut shell at ~~400 °C~~ 400 °C for ~~90~~90 min using a continuous flow of ~~500~~500 mL.min~~$^{-1}$~~$^{-1}$ of N_2 and a heating rate of ~~10 °C·min~~10 °C·min^{-1}. Then, a solution of Fe^{3+} was impregnated in **BC** in a 1: ~~1 weight~~ 1 wt ratio ($FeCl_3$~~·6H~~·6 H_2O / **BC**), dried, and then pyrolyzed at ~~500 °C~~ 500 °C under nitrogen ~~(500~~(500 mL·min~~$^{-1}$~~$^{-1}$) for ~~90~~90 min [18]. Then the soluble part was extracted with ultrapure water and dried in an oven. This product was named **MBC2**.

2.3 Production of magnetic nanocomposites

2.3.1 Preparation of activated biochar

To produce an activated biochar with high surface area and rich with mesoporous, phosphoric acid (H_3PO_4) was chosen as the activating agent. The concentrated acid was impregnated directly into the dry biomass in a ~~3:1 weight~~ 3:1 wt ratio (H_3PO_4 ~~[85~~[85 wt%] / biomass). The acid was added dropwise over the solid while the material was mixed using a pestle. The material was dried in an oven at ~~105 °C~~ 105 °C for ~~15~~15 h and cooled in a vacuum desiccator. The solid mixture was transferred to the pyrolysis reactor and heated at ~~500 °C~~ 500 °C for ~~2~~2 h under a constant flow rate of ~~500~~500 mL·min~~$^{-1}$~~$^{-1}$ of N_2. The solid obtained was continuously washed with ultrapure water and filtered [18]. Activated carbon / biochar prepared by this method was named **ACP**.

ACP was then triturated with a porcelain mortar and pestle and sieved through a series of sieves, separating, for the following steps, the fraction with granulometry ~~0.045~~0.045 mm~~mm < x < 0.150~~ < x < 0.150 mm, which was dried in an oven at ~~105 °C~~ 105 °C and stored in desiccators.

2.3.2 Preparation of magnetic nanoparticles (MNPs)

Iron (III) acetylacetonate was used as a metallic precursor. ~~8~~8 mmol of $Fe(C_5H_7O_2)_3$ was dissolved in ~~80~~80 mL of benzyl ether ($C_{14}H_{14}O$), along with ~~32~~32 mmol of oleic acid – a surfactant that acts to control particle size, as well as a coating agent – and ~~32~~32 mmol of oleylamine ($C_{18}H_{37}N$) which acts as a co-surfactant and mild reducing agent. The reaction occurred in a nitrogen atmosphere with stirring using a magnetic bar. A reflux apparatus in a tritubular flask with a thermocouple was used to control the temperature of the reaction medium. The mixture was heated to ~~300 °C,~~ 300 °C, and after ~~1~~1 h it was rapidly cooled to room temperature. The **MNPs** were precipitated in ethanol, separated with a neodymium magnet ($Nd_2Fe_{14}B$), and washed again with ethanol.

2.3.3 Preparation of magnetic nanocomposites

A sol ~~(3~~(3 mg·mL~~$^{-1}$~~$^{-1}$ of oleic acid@Fe_3O_4 in toluene) was selected for magnetic nanocomposites production after confirmation that the colloid would not break even with either centrifugation or by the action of a neodymium magnet for ~~16~~16 h. This material was then mixed with biochar in two different mass proportions (1:2 and 1:3) and at different contact times (5, 15, 30, 60, 90 e ~~120~~120 min). The discoloration of the suspension and the magnetic saturation value of the composite formed (**MNC**) were the parameters used to determine the ideal condition.

2.4 Characterization of the materials

The textural analysis of materials was examined through the adsorption of N_2 at ~~-196 °C~~ – 196 °C using a Micromeritics ASAP 2420 porosity analyzer. The Point of Zero Charge (pH_{PZC}) was determined by the pH drift method. For this, samples of ~~10.0~~10.0 mg of each biochar were added to flasks holding ~~30~~30 mL of an aqueous solution of ~~0.01~~0.01 mol·L^{-1} potassium chloride (KCl) with the pH value varying from 2 to 10. The flasks were put in a thermostatic bath with agitation (SW23 – Julabo) for ~~72~~72 h at ~~180~~180 rpm. Afterward, the final pH was measured and the pH_{PZC} was determined by plotting the data of the initial pH (pH_i) against the final pH (pH_f) and fitting the data with a 4th power equation. The point where the curve crosses the straight line of pH_i ~~= pH~~= pH_f is the pH_{PZC} of the material.

The synthesized **MBC1**, **MBC2**, **MNPs**, and composites were then characterized according to their crystalline phase using an X-ray diffractometer (XRD) by Bruker, model D8 Advance operating with a copper source, and a theta-theta goniometer with Bragg-Brentano geometry. In addition, the size of the material crystallites was estimated through Eq. 1, proposed by Scherrer [12].

$$d = \frac{k.\lambda}{\beta.\cos\ \theta} \quad (1)$$

The magnetic properties of the materials were investigated using a Superconducting Quantum Interference Device (SQUID) apparatus, model QD SX500 by Quantum Design. The magnetic behavior of the particles was analyzed by varying the applied field at a constant temperature ~~(300~~(300 K). The effect of varying the temperature from ~~5~~5 K to ~~300~~300 K was also studied after cooling the sample with or without an applied magnetic field, called ZfcFc (Zero-field-cooled / field-cooled) procedure.

The size and shape distribution of the MNPs and the formation of nanocomposites were studied by Transmission Electron Microscopy (TEM). The samples were suspended in toluene and subsequently deposited in copper grids coated with carbon in sample holders.

2.5 Chromatographic method

A chromatographic method was developed and validated to quantify the model contaminants (salicylic acid and caffeine) in water throughout the evaluation of the adsorption capacities of the produced materials in binary solutions. The method was developed using a high-performance liquid chromatography system with a diode array

detector (HPLC-DAD) equipped with a C18 analytical column (Phenomenex ~~50~~50 mm × 4.60 mm, ~~mm × 4.60~~ 3 µm, and pore size of ~~100~~100 Å). The injection volume was ~~10~~10 µL. Chromatographic separation was achieved using a mobile phase consisting of ~~10~~10 mmol·L$^{~~-1~~-1}$ ammonium acetate (pH 5.8) and methanol in a ratio of 70:30 (v/v). The flow rate was set at ~~0.6~~0.6 mL·min$^{~~-1~~-1}$.

2.6 Adsorption assays

All assays were conducted using each of the model contaminants separately and in the form of a binary mixture to evaluate better the interference that the presence of another substance may generate in the adsorption process.

2.6.1 Adsorption kinetics

Assays were conducted by adding 5 mL of a solution containing 45.0 mg·L$^{~~-1~~-1}$ of the model contaminant (salicylic acid and caffeine, either individually or in a mixture) into glass flasks containing approximately 5 mg of the analyzed adsorbent. The samples were maintained under agitation at 180 rpm and a temperature of 20 °C in a thermostatic bath with agitation (SW23 – Julabo). The contact time for each sample ranged from 1 min to 48 h, and each assay was performed in triplicate. After the specified time, the samples were filtered through a PTFE syringe filter (0.22 µm) and analyzed by HPLC-DAD to determine their concentration. Therefore, the adsorptive capacity (q_t), which represents the amount of pollutant adsorbed (mg) per gram of adsorbent for each test time, was calculated using the Eq. 2.

$$q_t = \left(\frac{C_0 - C_t}{m}\right) V \quad (2)$$

where C_0 is the initial concentration of the analyte studied; C_t is the concentration of analyte after the contact time t between the adsorbent and the analyte has elapsed; m is the mass of the analyte; and V is the volume of the studied solution. The kinetic adsorption was determined for all adsorbents using the q_t values. Pseudo-first order [19] and pseudo-second order [20] models, indicated in Eqs. 3 and 4, respectively, were considered for processing the data obtained. The non-linear equation data was adjusted through the Levenberg-Marquardt approximation method. The fitting of the equations to the data was evaluated by their adjusted R^2 and by the difference (Δq_e) between the q_e obtained experimentally (qe_{exp}) and the one calculated by the equations (qe_{calc}) according to the Eq. (5).

$$q_t = q_e \left[1 - \exp\left(-k_1 \cdot t\right) \right] \quad (3)$$

$$q_t = \frac{q_e^2 \cdot k_2 \cdot t}{1 + q_e \cdot k_2 \cdot t} \quad (4)$$

$$\Delta q_e = \frac{q_{e_{exp}} - q_{e_{calc}}}{q_{e_{exp}}} \quad (5)$$

2.6.2 Adsorption isotherms

Assays were performed by adding ~~5~~5 mL of a solution containing different concentrations of the model contaminant (salicylic acid and caffeine, individually or in a mixture) in glass flasks containing ~~5~~5 mg of the adsorbent. The samples were kept under stirring at ~~180~~180 rpm for ~~48~~48 h under controlled temperature ~~(20 °C)~~ (20 °C) in a bath with agitation. Each contaminant concentration was evaluated in triplicate. After incubation, the samples were filtered and then analyzed by HPLC-DAD. The experimental data were fitted to the Langmuir [21], Freundlich [22], and Sips [23] models, shown in Eqs. 6, 7, and 8.

$$q_e = \frac{Q_{max} \cdot K_L \cdot C_e}{1 + K_L \cdot C_e} \quad (6)$$

$$q_e = K_F \cdot C_e^{\left(\frac{1}{n}\right)} \quad (7)$$

$$q_e = \frac{Q_{max} \cdot K_S \cdot C_e^{m_S}}{1 + K_S \cdot C_e^{m_S}} \quad (8)$$

where Q_{max} is the maximum adsorption capacity, in [mg·g$^{~~-1~~-1}$]; K_L is the Langmuir equilibrium adsorption constant, [L·mg$^{~~-1~~-1}$]; n is a nondimensional constant of surface heterogeneity; K_F is the Freundlich adsorption capacity constant, in [mg·g$^{~~-1~~-1}$·(mg·L$^{~~-1~~-1}$)$^{~~-1/n~~-1/n}$]; K_S is the Sips equilibrium constant, in [(L·mg$^{~~-1~~-1}$)^{mS}]; and m_S is the Sips' model exponent.

3 Results and discussion

The currently available methodologies for producing magnetic biochar present certain limitations. One commonly used method involves the co-pyrolysis of biomass or biochar with iron salts. However, this approach has shortcoming in controlling particle size and crystallinity, and the obtained material often exhibits a poor magnetic response. In this study, two magnetic carbons were produced by the co-pyrolysis of green coconut husks with $FeCl_3$ **(MBC1)** and green coconut charcoal with $FeCl_3$ **(MBC2)**. Furthermore, an innovative methodology for obtaining magnetic carbons based on the combination of magnetic particles, synthesized by the method of thermal decomposition of an organometallic precursor, with activated carbon is presented. This approach aims to improve process control, enabling the production of activated carbons with high surface area and good magnetic properties. Fig. 1 presents a summary of the materials produced in this study.

alt-text: Fig. 1

Fig. 1

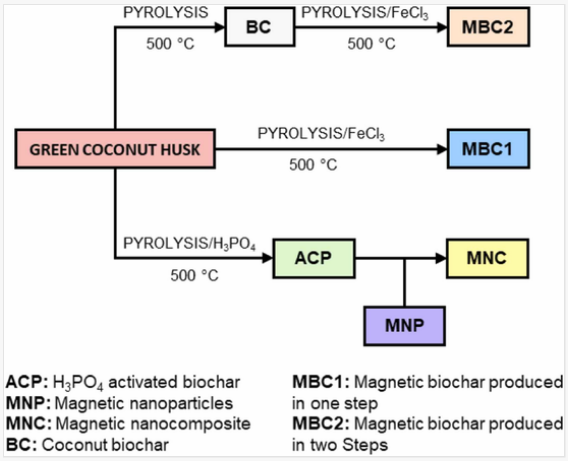

Summary of the materials presented in this study.

3.1 Biochars

During the activation process with H_3PO_4 in **ACP** production, the initial contact between biomass and phosphoric acid promotes a series of dehydration and carbonization reactions of part of the biomass, even before the pyrolysis process takes place. Subsequently, when the mixture enters the reactor and is heated to ~~500 °C,~~ 500 °C, the carbonization process occurs concurrently with acid degradation, generating a series of substances that, in turn, react with the lignocellulosic matter, participating in the intercrossing of intermediates formed during the process. Part of the phosphorus from activation remains in the carbonaceous matrix creating a series of C-O-P and P-C-O bonds, expanding the pore network of the material. Another part of the phosphorus remains in the form of water-soluble oxides and is washed away afterward. The removal of these soluble by-products, as well as the mineral part of the biomass that passed through digestion in an acid medium, creates vacancies in the remaining carbon matrix and thus increases, even more, the available surface [18,24].

ACP, along with other materials produced, was characterized based on their surface area, volume, and pore distribution. These characteristics play a crucial role in their application in pollutant adsorption and for incorporating nanoparticles in the activated carbon. Table 1 presents the difference between the coconut biochar produced through conventional slow pyrolysis **(BC)** and the activated carbon **(ACP)**. Notably, the activation process resulted in a significant enhancement in the porosity of the material, as evidenced by the specific area determined for the **ACP** ~~(1242 m~~(1242 $m^2 \cdot g^{-1}$~~)~~, which is substantially larger than that for the **BC** ~~(3 m~~(3 $m^2 \cdot g^{-1}$~~)~~. Furthermore, the shape of the **ACP** isotherm (Fig. 2) showed a type IV behavior, with an H4 hysteresis ending at approximately 0.4 relative pressure, showing a pore distribution divided between micropores and mesopores. This characteristic is extremely interesting for the preparation of magnetic composite since the mesopores can accommodate the magnetic nanoparticles effectively.

alt-text: Table 1

Table 1

The table layout displayed in this section is not how it will appear in the final version. The representation below is solely purposed for providing corrections to the table. To view the actual presentation of the table, please click on the Preview located at the top of the page.

Summary of textural and PZC analysis of prepared adsorbents.

Material	ACP	MNC	MBC1	MBC2	BC
BET surface area ($m^2 \cdot g^{-1}$)	1242	1019	474	338	3
t-plot micropore area ($m^2 \cdot g^{-1}$)	685	486	442	324	0.4
BJH pore volume ($cm^3 \cdot g^{-1}$)	0.973	0.839	0.039	0.020	0.002
Average pore diameter BJH (Å)	44	46	53	36	170
Point of zero charge pH_{PZC}	1.96	4.75	2.30	2.30	7.97

Images are optimised for fast web viewing. Click on the image to view the original version.

alt-text: Fig. 2

Fig. 2

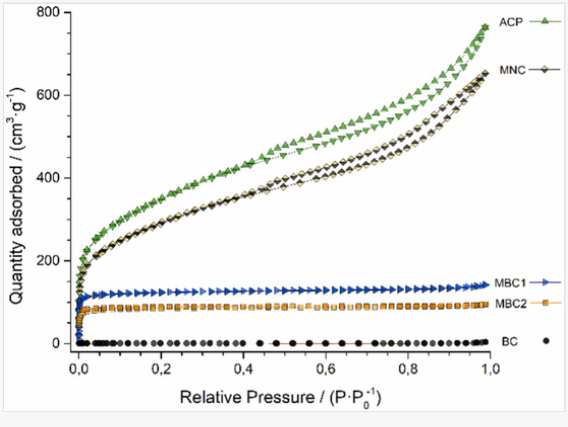

N_2 adsorption isotherms at ~~77~~77 K of the biochars.

Table 1 shows the results of the pH_{PZC} study of the produced biochars. In media with pH values lower than pH_{PZC}, the surface of the solid is positively charged. Similarly, media with a pH above pH_{PZC} have a negative surface charge. This charge on the material surface can hinder or assist in the adsorption. **BC** has a high pH_{PZC} because the material was not submitted to any activation process. However, the **ACP** has a low pH_{PZC}, possibly due to the introduction of oxygenated functional groups caused by mixing H_3PO_4 into the biomass.

3.2 Magnetic biochars

The magnetic biochars obtained from the co-pyrolysis of $FeCl_3$ with green coconut husks (**MBC1**) and green coconut charcoal **(MBC2)** were analyzed by X-Ray Diffraction (XRD) to evaluate the crystalline structure of the iron oxide compounds in their matrix. The diffractograms of the **MBC1** and **MBC2** products are shown in Fig. 3. The results confirm the presence of the magnetite/maghemite phase, which cannot be differentiated by XRD since they have the same inverse spinel crystalline structure.

alt-text: Fig. 3

Fig. 3

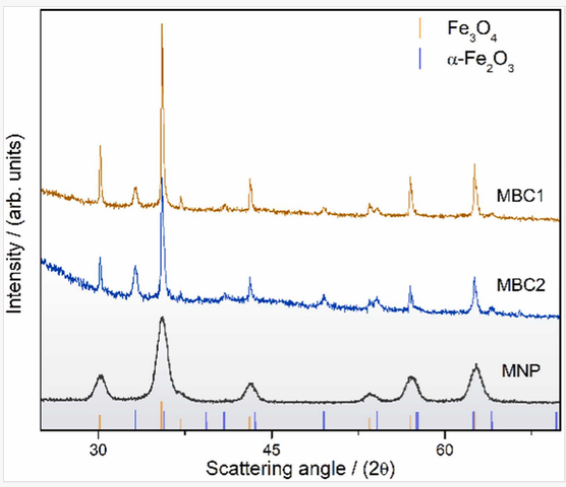

Diffractograms of magnetic nanoparticles and magnetic biochars.

Besides confirming magnetic iron oxides, residual hematite (α-Fe_2O_3) was observed in both materials. The presence of hematite, which is antiferromagnetic and exhibits a weak magnetic response, can impair the adsorbent recovery process after its use. The proportion between the amount of iron added and the mass of oxidizable carbon must be adjusted so that the formation of the spinel ferrite occurs to a greater extent by the reduction Fe^{3+} ions by the carbon. However, this appears to be an inherent challenge in this type of synthesis as the thermal reaction of iron reduction using lignocellulosic biomass or biochar is difficult to control at this low temperature range ~~(300–500 °C),~~ (300–500 °C), resulting in the inability to obtain pure magnetite and maghemite, which are metastable phases. Similar findings have been reported in numerous studies utilizing this synthesis approach [17,25,26].

MBC2 and **MBC1** exhibited a magnetization of ~~5.1~~5.1 emu·g~~-1~~$^{-1}$ and ~~11.9~~11.9 emu·g~~-1~~$^{-1}$, respectively. The different magnetization values can be associated with the distinct synthesis processes employed for each material. **MBC2** synthesis involved starting from a previously carbonized material **(BC)**, while **MBC1** utilized unaltered green coconut biomass. The distribution of solid, liquid, and gaseous products for **MBC1** was 54%, 25%, and 22%, respectively. On the other hand, for **MBC2**, the distribution was 67% solid, 12% liquid, and 21% gaseous products. Thus, **MBC1** has a higher Fe/C ratio compared to **MBC2**, despite both processes using the same amount of Fe^{3+} and starting material.

Table 2 presents surface area and saturation magnetization data from other studies that utilized the co-pyrolysis method to produce magnetic carbons. The results indicate that the obtained materials demonstrated satisfactory magnetization levels; however, their surface areas were considered inadequate for their potential application as adsorbents in contaminated water treatment. Hence, it is evident that the **MBC1** and **MBC2** carbons, synthesized as reference materials for evaluating the proposed novel method, align with the observed trends associated with the co-pyrolysis technique, where controlling material porosity represents a significant challenge.

alt-text: Table 2

Table 2

Surface area and saturation magnetization data of magnetic carbons produced by the co-pyrolysis method.

Feedstock	Method	Characteristics	Ref
Sawdust	• Mass ratio of $FeCl_3$~~·6H~~·6 H_2O to sawdust of 0.5; 1; 1.5; or 2 •	**BET surface area:** 27.08–164.94 $m^2 \cdot g^{-1}$	[27]

	Pyrolysis for ~~1 h~~ 1 h at 500; 600; 700; or ~~800 °C~~800 °C	**Saturation magnetization:** ± 55 emu·g$^{~~-1~~-1}$	
Eucalyptus sawdust	• Mass ratio of $FeCl_3$ to eucalyptus sawdust of 2:1 • Calcination for ~~75~~75 min at ~~700 °C~~700 °C	**BET surface area:** 645.23 $m^2 \cdot g^{~~-1~~-1}$ **Saturation magnetization:** 30.37 emu·g$^{~~-1~~-1}$	[28]
Tea residue powder (TRP)	• Mass ratio of $FeCl_3$~~·6H~~·6 H_2O to TRP of 1.35 • $FeCl_3$-loaded TRP powder Mixed with KOH in various ratios (m_{KOH}:m_{FeT} = 0, 0.2, 0.5, 1) • Pyrolysis for ~~2~~2 h at ~~700 °C~~700 °C	**BET surface area:** 409.15 $m^2 \cdot g^{~~-1~~-1}$ **Saturation magnetization:** 19.69 emu·g$^{~~-1~~-1}$	[29]
Rice husk sample after hydrothermal and alkali pretreatments	• Mass ratio of $FeCl_3$~~·6H~~·6 H_2O to Rice husk or NaOH treated hydrochar of 0.2 • Pyrolysis for ~~+~~1 h at ~~600 °C~~600 °C	**BET surface area:** 454.6 $m^2 \cdot g^{~~-1~~-1}$ **Saturation magnetization:** 11.62 emu·g$^{~~-1~~-1}$	[30]
Carbonized coconut shell (Cb)	• Mass ratio of $FeCl_3$~~·6H~~·6 H_2O to Cb of 1; 2; or 3 • Pyrolysis for ~~1.5~~1.5 h at ~~700 °C~~700 °C	**BET surface area:** 6 – 238 $m^2 \cdot g^{~~-1~~-1}$ **Saturation magnetization:** 16.55–28.74 emu·g$^{~~-1~~-1}$	[31]

3.3 Production and characterization of magnetic nanoparticles

Among the potential approaches for producing a nanocomposite of biochar and magnetite nanoparticles, we selected synthesizing the two components separately and combining them later. This approach aims towards better control over both processes and obtain a material that can be easily adaptable to different requirements.

Magnetic nanoparticles (MNPs) were produced by the thermal decomposition of an organometallic precursor, using a surfactant for size control and as a mild reducing agent. This methodology is well-known for yielding materials with good crystallinity, size control, and magnetic response [32]. When selecting the synthesis approach, another crucial factor considered was the desired size of the magnetite nanoparticles (MNPs). Since the aim was to incorporate the MNPs within the pores of biochars, it was necessary for the nanoparticles to be sufficiently small, as most of the pores in these materials are below ~~50~~50 nm (Table 1). However, neither could the magnetite particles be excessively small, for two reasons: I) if they were small enough to penetrate all the pores they could overload the porosity of the biochar, making the application of contaminant adsorption unfeasible; and II) very small particles may affect the magnetic properties of the composite.

The oleic acid added to the reaction served two purposes. After primary nucleation, oleic acid forms an organic shell around the crystals which acts as a protective layer, covering the nanoparticles and preventing them from forming aggregates. This protective layer also prevents secondary nucleation from occurring. It does not allow the crystal to continue growing indefinitely and thus works as a size controller during synthesis.

The product was also studied by powder X-ray diffraction (Fig. 3), and it is possible to verify that there was no crystalline phase other than that of maghemite and/or magnetite. In addition, it was possible to use the diffractogram to estimate the size of these material crystallites, which showed that the average diameter is ~~11.2 ± 1.1~~11.2 ± 1.1 nm.

The MNPs morphological characterization, performed through Transmission electron microscopy, displayed that the magnetic nanoparticles produced were monocrystalline – with an average diameter similar to that obtained through XRD with Scherrer's equation (1918). A population of 300 particles was computed to estimate the mean diameter, obtaining the mean value of ~~11.4 ± 2.2~~11.4 ± 2.2 nm for one of the batches, illustrated in Fig. 4.

Images are optimised for fast web viewing. Click on the image to view the original version.

alt-text: Fig. 4

Fig. 4

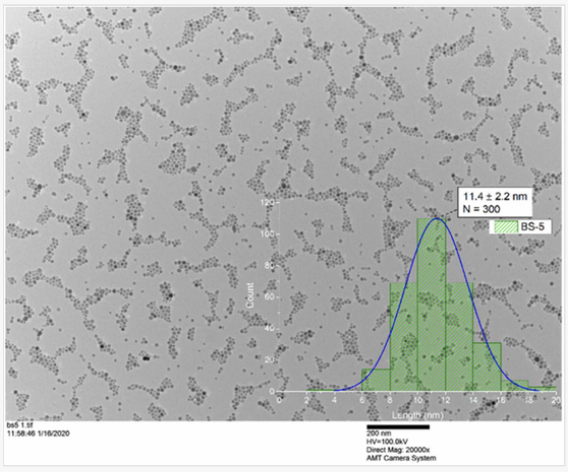

Transmission Electron Micrograph of MNPs with 20000x zoom and particle diameter distribution.

Four batches of magnetite nanoparticles coated with oleic acid were synthesized and little variation was observed between processes. The average yield of each batch of MNPs was ~~88% ± 9%,~~ 88% ± 9%, the average magnetic saturation was ~~67.4 ± 2.6~~67.4 ± 2.6 emu·g$^{~~-1~~-1}$, and the average crystallite size was ~~11.2 ± 1.1~~11.2 ± 1.1 nm. Therefore, it can be concluded that different batches of the material can be used with good reproducibility. The similar size obtained by TEM and XRD analyses leads us to conclude that the synthesized particles have good crystallinity, which directly impacts the material magnetic properties.

The average magnetic saturation of the synthesized MNPs was ~~67.4 ± 2.6~~67.4 ± 2.6 emu·g^{-1}~~−1~~. The magnetization curve displayed in Fig. 5 evidences an almost non-existent hysteresis, with a coercivity of ~~10~~10 Oe and a remanence of ~~1.3~~1.3 emu·g^{-1}~~−1~~, demonstrating a characteristic very close to ideal superparamagnetism, when there is no magnetic hysteresis, and the remanent magnetization is zero.

alt-text: Fig. 5

Fig. 5

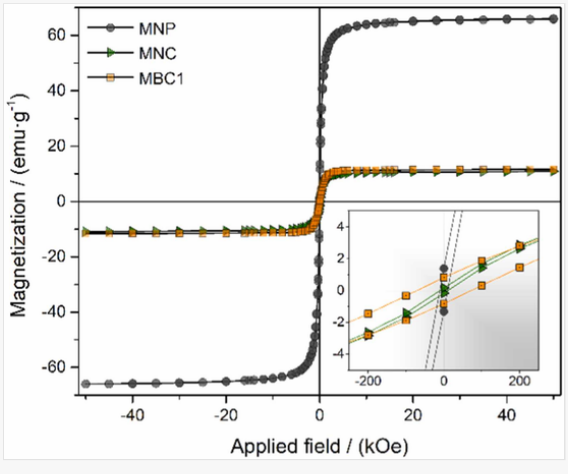

Magnetization hysteresis loop of the materials **MNP**, **MBC1**, and **MNC**.

3.4 Production of magnetic nanocomposite

The use of a stable colloidal solution was chosen to prevent the formation of clusters of isolated **MNPs** and to enhance the contact between the **MNPs** and **ACP**. To the best of our knowledge, this is the first report utilizing this methodology. By placing the **ACP** biochar in contact with the sol, the **MNPs** were extracted from the toluene media, and the resulting composite was subsequently attracted by the permanent magnet. The conditions established for obtaining the colloid ~~(3~~(3 mg·mL^{-1}~~−1~~ in toluene) aimed at not wasting magnetic material, ensuring control over the mass of **MNPs** involved in the process.

Transmission Electron Microscopy analysis (Fig. 3b, c, and d) showed that the **MNPs** remained adhered to the biochar surface even after sample preparation for TEM with ultrasound irradiation. Fig 6.

alt-text: Fig. 6

Fig. 6

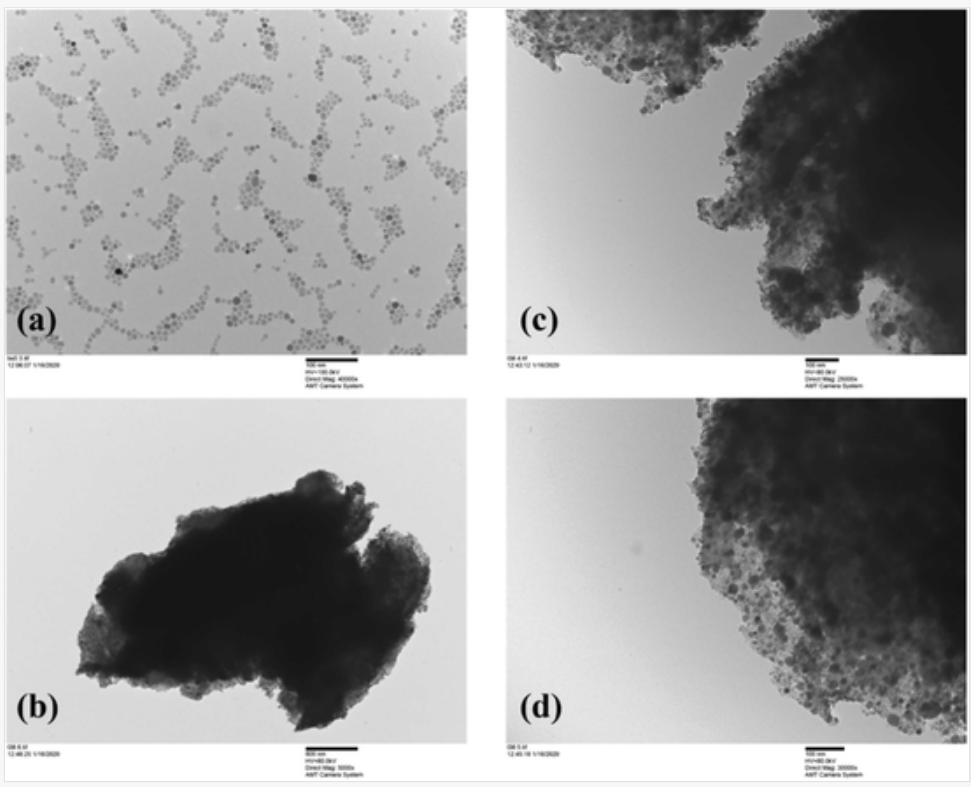

Transmission Electron Micrograph of MNPs with 40000x zoom **(a)**; and of the **MNC** with 5000x **(b)**, 25000x **(c)**, and 30000x **(d)**.

The role of the relative amount of **MNP** to **ACP** in the magnetic nanocomposite preparation - (1:2 and 1:3, **MNP**:**ACP**, w/w) – and of the contact times (5, 15, 30, 60, 90, and ~~120~~120 min) was investigated. The results exhibited no increase in magnetization when increasing the proportion of **MNPs** to carbon from ~~1:3 to 1:2.~~ 1:3–1:2. Regarding contact time, the results revealed a poor increment in magnetization value after ~~15~~15 min of contact (Fig. 7) suggesting that the maximum loading was reached.

alt-text: Fig. 7

Fig. 7

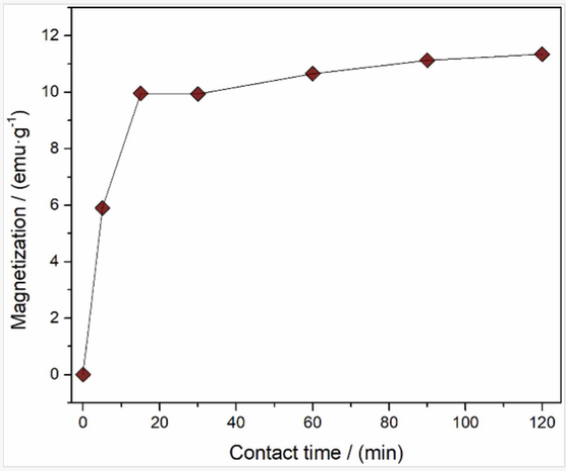

Magnetization as a function of the contact time between the **ACP** and the sol.

Five batches of the magnetic nanocomposite were produced using the proposed final condition: a 1:3 mass ratio between **MNPs** and **ACP** biochar, using a colloid with a concentration of ~~3~~3 mg·mL^{-1}, and a contact time of ~~15~~15 min. The average magnetization obtained in the nanocomposite was ~~11.2 ± 1.1~~11.2 ± 1.1 emu·g^{-1}. The coefficient of variation in the magnetic response was 10%, showing that the nanocomposite synthesis is quite reproducible. Therefore, all batches were mixed, and the material, called **MNC**, was tested as a potential adsorbent of contaminants in water.

3.5 Comparison of the materials

When comparing the porosity of all synthesized materials by the N_2 adsorption isotherm (Table 1), the exciting potential of the proposed new methodology is strengthened. Despite a slightly reduction in pore volume and specific surface, the **MNC** nanocomposite maintained much of the porosity ~~(0.839 cm~~(0.839 cm^3·g^{-1}) of the **ACP** biochar ~~(0.973 cm~~(0.973 cm^3·g^{-1}) which is essential for its application. Also, **MNC** maintained the type IV isotherm shape with type H4 hysteresis ending at a relative pressure of approximately 0.4 (Fig. 2).

The feasibility of the methodology for **MBC1** and **MBC2** synthesis should be highlighted. These materials were prepared through the traditional method of impregnation of the starting material with iron (III) followed by its pyrolysis, furnishing the magnetic material simultaneously with the chemical activation of the carbonaceous material. **MBC1** and **MBC2** showed a considerable increase in their specific surfaces compared to non-activated **BC** biochar. Both materials showed similar adsorption isotherms, type IV with very narrow hysteresis, and a significant similarity to the type I isotherm and exhibit predominantly micropores. However, **MBC1** biochar exhibited a higher specific surface than **MBC2**. Because of this, it was chosen to serve as a comparison with **MNC** in the application tests as an adsorbent.

Another important feature of a magnetic adsorbent is its superparamagnetic character. In the case of the studied materials, the remnant magnetization was extremely low, being ~~0.8~~0.8 emu·g^{-1} for the **MBC1** magnetic carbon and ~~0.2~~0.2 emu·g^{-1}, for the **MNC** nanocomposite, as shown in the inset of Fig. 5.

3.6 Adsorption studies

3.6.1 Adsorption kinetics

Different kinetic models have been used to describe the adsorption of organic contaminants on activated carbon, but in most cases, the pseudo-first-order and pseudo-second-order models fit well within the adsorption behavior of the experiments described in the literature. Therefore, these models were used to compare the process kinetics of the produced materials.

According to Revellame et al., 2020 [33], values of $R^2 > 0.8$ for the non-linear regression of each model indicate a good correlation between the experimental data and the kinetic models. However, there is a need for more parameters to establish which model is more representative of the analyzed system. The difference (Δq_e) between the values calculated for the amount of contaminant adsorbed at equilibrium (qe_{exp}) and the values found experimentally (qe_{calc}) can be used for this purpose. A smaller difference reveals a better fit of the model to the experimental data. The pseudo-second order model better describes the adsorption of solids rich in active sites, while the opposite occurs for the pseudo-first order model [34].

The adsorption of salicylic acid (SA) individually by **MBC1** follows the pseudo-second order model (Table 3), since this model presented higher R^2 values and lower Δq_e values, indicating a better fit to the experimental data. This indicates that adsorption is the limiting step of the process since the material has a high surface area. However, in the binary mixture, there is less surface area available for the adsorption of SA since the other contaminant molecules fill part of the material surface. Thus, the data fits better in the model of pseudo-first order at the binary mixture, which means that external or intraparticle diffusion is the slow step of the adsorption. On the other hand, it was not possible to distinguish which model is more representative of the adsorption of caffeine (CAF) individually or in the binary mixture. **MBC1** exhibited low adsorption efficiency for CAF, making it challenging to determine the most suitable experimental model for data fitting.

alt-text: Table 3

Table 3

The table layout displayed in this section is not how it will appear in the final version. The representation below is solely purposed for providing corrections to the table. To view the actual presentation of the table, please click on the Preview located at the top of the page.

Adjustment of kinetic models to experimental data for caffeine (CAF) and salicylic acid (SA) adsorption.

Biochar	Analyte	Pseudo-first order					Pseudo-second order				
		qe_{exp} [mg·g^{-1}]	qe_{calc} [mg·g^{-1}]	k_1 [s^{-1}]	R^2	Δq_e%	qe_{exp} [mg·g^{-1}]	qe_{calc} [mg·g^{-1}]	k_2 [s^{-1}]	R^2	Δq_e %
MBC1	SA	39	36	0	0.89	7.7	39	38	5.8	0.95	2.6
	SA (bin)	35	35	7.2·10^{-3}	0.93	0	39	37	2.9·10^{-4}	0.91	5.1
	CAF	15	16	8.0·10^{-3}	0.84	-6.7	15	17	6.6·10^{-4}	0.89	13.3
	CAF (bin)	6	7	4.9·10^{-3}	0.88	-16.7	6	8	4.6·10^{-4}	0.91	-33.3
ACP	SA	39	39	2.5	0.98	0.0	39	38	0.2	0.98	2.6
	SA (bin)	39	38	2.1	0.95	2.6	39	39	1.3·10^{-1}	0.96	0.0

	CAF	36	33	1.5	0.90	8.3	36	33	$7.0 \cdot 10^{-2}$	0.93	8.3
	CAF (bin)	32	38	1.2	0.83	-18.8	32	29	$4.6 \cdot 10^{-2}$	0.89	9.4
MNC	SA	25	22	1.0	0.80	12.0	25	23	$4.4 \cdot 10^{-2}$	0.81	8.0
	SA (bin)	21	19	0.9	0.70	9.5	21	20	$3.3 \cdot 10^{-2}$	0.87	4.8
	CAF	36	34	1.3	0.90	5.6	36	35	$5.2 \cdot 10^{-2}$	0.89	2.8
	CAF (bin)	36	34	1.3	0.90	5.6	36	35	$5.2 \cdot 10^{-2}$	0.89	2.8

The adsorption of SA and CAF, whether individually or in a binary mixture, by **MNC** and **ACP**, is better represented by the pseudo-second order model. This is supported by the R^2 and Δq_e parameters presented in Table 3. In this particular case, both **MNC** and **ACP** exhibit significantly high surface areas, indicating the presence of a large number of active sites, as suggested by the pseudo-second order model. Moreover, the adsorption sites on the surface of the material are less affected by another contaminant in the solution than by **MBC1**, which has a significantly lower surface area. Consequently, adsorption at the active sites becomes the rate-limiting step in all the analyzed scenarios.

3.6.2 Adsorption isotherms

The investigation of adsorption isotherms provides a relationship between the contaminant concentration in the solution and the amount of adsorbate on the solid phase when both phases reach equilibrium at a specific temperature. Mathematical models are used to fit the adsorption isotherm experimental data in order to obtain insights regarding the sorption mechanism, surface properties, and the interaction between the adsorbate and the adsorbent. In this study, three isotherm models were used via non-linear regression methods to elucidate the equilibrium data: the two-parameter models Langmuir and Freundlich, and three-parameter model Sips. The calculated parameter coefficient for Langmuir, Freundlich, and Sips isotherm models are presented in Table 4.

alt-text: Table 4

Table 4

The table layout displayed in this section is not how it will appear in the final version. The representation below is solely purposed for providing corrections to the table. To view the actual presentation of the table, please click on the Preview located at the top of the page.

Adjustment of isotherm models to experimental data.

Biochar	**Analyte**	**Sips**				**Langmuir**			**Freundlich**		
		Q_{max} [mg·g^{-1-1}]	**K_S (L·mg^{-1-1})^{mS}**	**m_s**	**R^2**	**Q_{max} [mg·g^{-1-1}]**	**K_L [L·mg^{-1-1}]**	**R^2**	**n**	**K_F mg·g^{-1-1}· (L·mg^{-1-1})$^{1/n}$**	**R^2**
MBC1	SA	111	0.13	0.43	0.9963	95.27	0.16	0.9449	7.07	40.10	0.9314
	SA (bin)	109	0.055	0.29	0.9688	74.85	0.21	0.7564	6.68	32.53	0.9571
	CAF	45	0.01	0.41	0.9866	30	0.046	0.9472	5.05	8.73	0.9773
	CAF (bin)	-	-	-	-	-	-	-	-	-	-
ACP	SA	521	$1.6 \cdot 10^{-3-3}$	0.59	0.9976	121	0.091	0.9400	1.87	11.38	0.9931
	SA (bin)	519	$1.8 \cdot 10^{-5-5}$	0.46	0.9952	118	0.10	0.8935	2.24	9.86	0.9956
	CAF	259	$4.8 \cdot 10^{-2-2}$	0.46	0.9976	182	0.49	0.9586	4.01	49.77	0.9805
	CAF (bin)	159	$1.9 \cdot 10^{-1-1}$	1.16	0.9464	143	0.32	0.9392	2.55	18.24	0.7589
MNC	SA	233	$6.35 \cdot 10^{-3-3}$	0.85	0.9993	178	0.013	0.9992	1.70	5.72	0.9956
	SA (bin)	291	$1.51 \cdot 10^{-3-3}$	0.70	0.9850	135	0.011	0.9592	1.72	3.84	0.9790
	CAF	168	0.069	0.52	0.9947	148	0.25	0.9935	4.06	37.90	0.9615
	CAF (bin)	111	1.24	2.59	0.9957	113	0.56	0.9939	3.65	29.55	0.9896

Comparing the adsorptive capacity (Fig. 8) of **MBC1** for both model contaminants, the expressive interaction of the adsorbent with SA is highlighted. The binary assays resulted in the reduction of the adsorptive capacities for CAF and SA, but the higher amount of SA adsorbed still stands out. The iron oxides (α-Fe_2O_3, Fe_3O_4, and/or γ-Fe_2O_3) present in biochar may be related to the higher adsorption capacity of SA compared to CAF on **MBC1**. Magnetite particles show a significant interaction with carboxylates present in SA structure due to the bidentate -O-C-O- interaction with the oxide surface. Therefore, it is reasonable to assume that iron oxides significantly contribute to the adsorption of SA [35,36].

Images are optimised for fast web viewing. Click on the image to view the original version.

alt-text: Fig. 8

Fig. 8

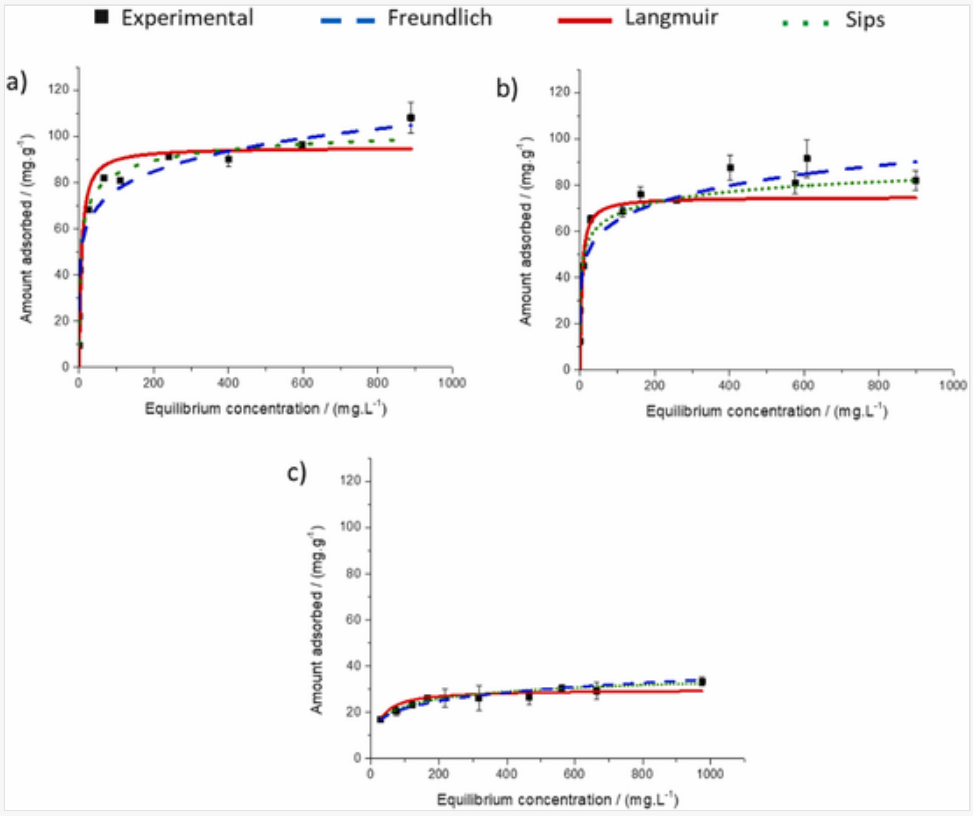

MBC1 adsorption isotherms with SA **(a)**; SA **(b)** in binary mixture adsorption; and CAF **(c)**.

It is worth mentioning that the adsorption of CAF in the binary mixture occurred at very low levels, making it impossible to observe the formation of the isotherm curve. Even at the lowest concentrations evaluated, the biochar was promptly saturated. One hypothesis for this limited adsorption capacity of CAF is the presence of relatively large and abundant iron oxide particles on the surface of the **MBC1** biochar, which prevent access to the inner surface of the carbonaceous network. On the other hand, the interaction of SA and iron oxides allows its adsorption without the need to diffuse deeply through the biochar pores [37].

The adjusted coefficient of determination (R^2_{adj}) values presented in Table 4 indicate that the Sips model exhibits a better fit to the adsorption of SA and CAF by **MBC1**. According to the Langmuir model, the solid surface is energetically homogeneous, and adsorption occurs with the formation of a monolayer of adsorbate on the adsorbent surface. On the other hand, the Freundlich model suggests that the solid surface is energetically heterogeneous, resulting in the formation of multilayers of adsorbate on the adsorbent surface. The Sips model combines these two models, in which the adsorption is diffusion controlled at low SA and CAF concentrations, while presenting a finit limit at high contaminant concentrations, as if in a monolayer [38].

The m_s parameter obtained from the Sips model is used to assess the heterogeneity of the solid surface. A value close to 1 indicates a more homogeneous surface, whereas values significantly different from 1 suggest surface heterogeneity. In the case of **MBC1**, the m_s values deviate significantly from 1, indicating a highly heterogeneous surface. This observation aligns with the presence of components such as Fe_2O_3, Fe_3O_4, and C on the **MBC1** surface.

ACP exhibited a higher CAF adsorption capacity compared to the other materials, as evidenced by the Q_{max} values of the Sips and Langmuir models (Table 4). All the analyzed materials have acidic characteristics, presenting a negative charge at the water pH, and it is not possible to differentiate their adsorptive capacities based on this parameter. Consequently, the higher adsorption capacity of CAF on **ACP** can be attributed to its larger surface area.

Upon comparing the Q_{max} values for the adsorption of CAF and SA on **ACP**, it can be observed that this adsorbent exhibits a higher adsorption capacity for SA, despite not having iron oxides particles. Since the presence of a preferential adsorption site is not present, unlike the magnetic materials, the adsorption of SA readily forms multilayers inside the carbon pores. The unexpectedly large Q_{max} values for SA obtained from the Sips equation are a reflection of this behavior. Since it leads to an adsorption isotherm with no clear plateau and a Q_{max} value that is difficult to predict reliably.

Similar to the behavior observed in **MBC1**, the analysis of R^2 values in Table 4 for **ACP** reveals that the Sips model provides a better fit to the experimental data. The adsorption isotherms of **ACP** (Fig. 9) demonstrate that Freundlich model deviate from the experimental values, particularly at high adsorbate concentrations. Additionally, the m_s parameters obtained from Sips model indicate that the surface of the solid is relatively heterogeneous. Since the Langmuir model assumes a perfectly homogenous adsorbent surface, the Sips model is the most suitable for describing the adsorption of CAF and SA, individually and in the binary mixture, on **MBC1**. Biochar, despite being predominantly composed of carbon, exhibits various functional groups on its surface. The presence of different chemical functional groups with varying polarities may account for the non-homogeneous behavior observed.

alt-text: Fig. 9

Fig. 9

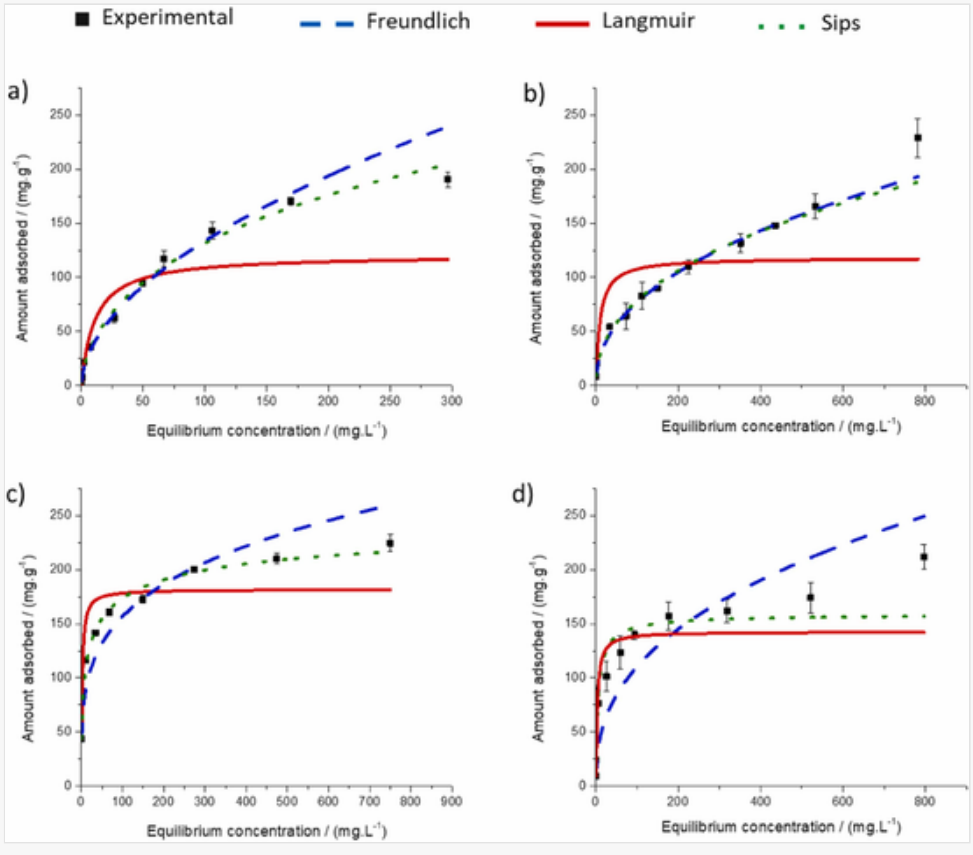

ACP adsorption isotherms with SA **(a)**; SA in binary mixture adsorption **(b)**; CAF **(c)**; and CAF in binary mixture adsorption **(d)**.

MNC exhibited a higher capacity to adsorb SA in comparison to the CAF, as evidenced by the Q_{max} values obtained from the Langmuir and Sips models (Table 4). In addition, the Q_{max} values obtained from the Langmuir model highlight that **MNC** is the most effective adsorbent for SA, in comparison to **ACP** and **MBC1**. As discussed for **MBC1**, the presence of magnetic particles on the adsorbate surface can enhance SA adsorption through interactions between the carboxylates present in SA and the oxide surface. Moreover, **MNC** exhibited higher surface area than **MBC1**, resulting in an increment in the SA adsorption capacity.

Upon analyzing the R^2_{adj} values (Table 4) and the deviation of each model from the experimental data (Fig. 10), the Sips model demonstrated the best fit for the SA and CAF adsorption at the evaluated concentration range. The m_s values for **MNC** are closer to 1, indicating a more homogeneous surface compared to the other materials. Interestingly, the Langmuir model showed higher R^2 values for **MNC** in comparison to **MBC1** and **ACP**, supporting the presence of a more homogenous surface. One possible explanation for this greater homogeneity in **MNC** could be attributed to the smaller size of the magnetite nanoparticles present on its surface.

alt-text: Fig. 10

Fig. 10

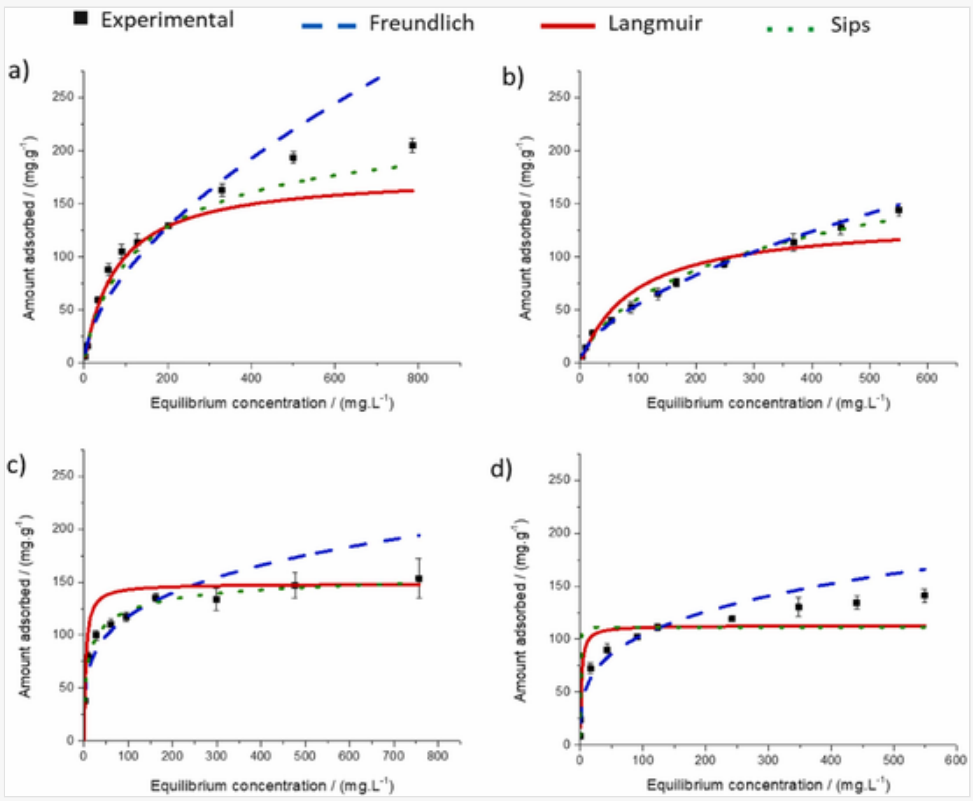

MNC adsorption isotherms with AS **(a)**; AS **(b)** in bicomponent adsorption; CAF **(c)**; and CAF in bicomponent adsorption **(d)**.

As highlighted earlier, the **MNC** adsorbent obtained using the novel method proposed in this study exhibited higher surface area and magnetization compared to other magnetic carbons reported in the literature (Table 2). The adsorption studies allowed us to evaluate the environmental application impact of the new adsorbent. Considering the Q_{max} values obtained from the Sips model, the maximum adsorption capacity for adsorption of CAF on **MNC** (148 mg·g^{-1}) was higher than those obtained for the same contaminant model using as adsorbent: commercial activated carbon (88 mg·g^{-1}) [39], fique bagasse modified biochar (80·65 mg.g^{-1}) [40], and activated carbon from *Elaeis guineensis* (13.5 mg·g^{-1}) [41]. The Q_{max} value obtained for adsorption of AS on **MNC** was 178 mg·g^{-1}, demonstrating the superior performance of this adsorbent compared to pine wood biochar (8–23 mg·g^{-1}) [42], commercial activated carbon (33 mg·g^{-1}) [39], and biochar from wood (48–51 mg·g^{-1}) [43].

Thus, the efficacy of the novel method proposed for synthesizing magnetic activated carbons is evident, as it yields a material with exceptional adsorbent properties. Additionally, its magnetic nature provides the advantage of facile separation from the reaction medium. These results strongly suggest that the proposed production method represents a valuable tool for advancing the development of innovative magnetic adsorbent materials.

4 Conclusion

An innovative method was developed for synthesizing magnetic carbons in order to obtain materials with more controlled properties, high surface area, and good magnetization. In this approach, a magnetic nanocomposite (**MNC**) was developed by combining an oleic acid coated magnetite colloid with green coconut husk biochar activated with H_3PO_4 (**ACP**). In addition, two other magnetic carbons were prepared by co-pyrolysis of $FeCl_3$ with green coconut husk biomass (**MBC1**) and with green coconut husk biochar (**MBC2**) according to methods already reported in the literature as a reference.

MNC, the magnetic nanocomposite produced by the novel method, presented a notable surface area ~~(1019 m~~(1019 m^2/g), demonstrating that the deposition of magnetic nanoparticles on **ACP** biochar surface did not significantly affect its surface area ~~(1242 m~~(1242 m^2/g). In contrast, the surface area obtained for **MBC1** and **MBC2** was ~~474 m~~474 m^2·g^{-1} and ~~338 m~~338 m^2·g^{-1}, respectively. Furthermore, the saturation magnetization of **MNC** ~~(11.2~~(11.2 emu·g^{-1}) was comparable to that of **MBC1** ~~(11.9~~(11.9 emu·g^{-1}) and higher than that of **MBC2** ~~(5.1~~(5.1 emu·g^{-1}). Finally, **ACP** and **MNC** showed considerably higher adsorptive capacities than **MBC1**. For caffeine adsorption, **ACP** proved to be the best adsorbent, possibly due to its larger surface area. As for the adsorption of salicylic acid, according to the Langmuir model, **MNC** was superior, possibly due to its high surface area combined with contaminant interactions with magnetic nanoparticles.

These findings support the feasibility of the novel method for producing magnetic biochar, which furnishes cost reduction in wastewater treatment by facilitating the removal of adsorbents from the liquid phase. Furthermore, the obtained adsorbent demonstrated high adsorption capacity, showing promising potential as an alternative for water contaminant remediation. Additionally, utilizing green coconut husk residues contributes to cost reduction and offers a sustainable solution for managing solid waste that might otherwise accumulate in nature and cause environmental issues. In the future, the materials produced can be evaluated for their adsorption capacity under real conditions. Furthermore, it is possible to assess whether the proposed method could be applied to biochars with different characteristics, such as those derived from other types of biomasses and/or that underwent other types of activation.

CRediT authorship contribution statement

Bruno Salarini Peixoto : Conceptualization, Methodology, Formal analysis, Investigation, Resources, Writing – original draft, Writing – review & editing, Visualization. **Larissa Silva de Oliveira Mota :** Methodology, Formal analysis, Investigation, Resources, Writing – original draft, Writing – review & editing, Visualization. **Isac Marinho Dias :** Methodology, Formal analysis, Investigation. **Beatrice Muzzi :** Methodology, Formal analysis, Investigation. **Martin Albino :** Methodology, Formal analysis, Investigation. **Michele Petrecca :** Methodology, Formal analysis, Investigation. **Claudia Innocenti :** Supervision, Funding acquisition. **Pamella Christina Ortega de Oliveira :** Investigation, Visualization. **Gilberto Alves Romeiro :** Investigation, Supervision. **Claudio Sangregorio :** Resources, Writing – original draft, Writing – review & editing, Visualization, Supervision, Funding acquisition. **Marcela Cristina de Moraes :** Conceptualization, Methodology, Resources, Visualization, Supervision, Project administration, Funding acquisition.

Declaration of Competing Interest

The authors declare that they have no known competing financial interests or personal relationships that could have appeared to influence the work reported in this paper.

Q3 Acknowledgments

This study was financed in part by the Coordenação de Aperfeiçoamento de Pessoal de Nível Superior - Brazil ~~(CAPES)~~(CAPES) within the scope of the Capes-PrInt Program - Universidade Federal Fluminense - Financial Code 001~~001,~~, project numbers 88887.310269/2018-00 and 88887.571298/2020-00~~88887.571298/2020-00,~~. M.C.M, B.S.P., and L.S.O.M. gratefully acknowledge Fundação Carlos Chagas Filho de Amparo à Pesquisa do Estado do Rio de Janeiro - FAPERJ (Grants E-26/200.584/2021~~E-26/200.584/2021;~~; E-26/010.000978/2019~~E-26/010.000978/2019,~~, E-26/200.285/2019~~E-26/200.285/2019,~~, SEI-260003/001167/2020~~SEI-260003/001167/2020,~~, and E-26/200.172/2023~~E-26/200.172/2023).~~). ~~Declaration of Competing InterestThe authors declare that they have no known competing financial interests or personal relationships that could have appeared to influence the work reported in this paper.~~

References

The corrections made in this section will be reviewed and approved by a journal production editor. The newly added/removed references and its citations will be reordered and rearranged by the production team.

[1] J. Kapelewska, U. Kotowska, J. Karpińska, D. Kowalczuk, A. Arciszewska, A. Świrydo, Occurrence, removal, mass loading and environmental risk assessment of emerging organic contaminants in leachates, groundwaters and wastewaters, Microchem. J. 137 (2018) 292–301, doi:10.1016/j.microc.2017.11.008.

[2] S. Khan, Mu Naushad, M. Govarthanan, J. Iqbal, S.M. Alfadul, Emerging contaminants of high concern for the environment: Current trends and future research, Environ. Res. 207 (2022) 112609, doi:10.1016/j.envres.2021.112609.

[3] B.S. Peixoto, L.S. de, O. Mota, P.C.O. de Oliveira, M.C. da, C. Veloso, G.A. Romeiro, M.C. de Moraes, Highly functionalized microporous activated biochar from syagrus coronata waste: production, characterization, and application in adsorption studies, Water 14 (2022) 3525, doi:10.3390/w14213525.

[4]

C. Sophia, A, E.C. Lima, Removal of emerging contaminants from the environment by adsorption, Ecotoxicol. Environ. Saf. 150 (2018) 1–17, doi:10.1016/j.ecoenv.2017.12.026.

[5] M. Varsha, P. Senthil Kumar, B. Senthil Rathi, A review on recent trends in the removal of emerging contaminants from aquatic environment using low-cost adsorbents, Chemosphere 287 (2022) 132270, doi:10.1016/j.chemosphere.2021.132270.

[6] A.F. Abou-Hadid, U.A. El-Behairy, M.M. Elmalih, E. Amdeha, A.M.A.E. Naggar, M.H. Taha, A.E.M. Hussein, Conversion of corn shell as biomass solid waste into carbon species for efficient decontamination of wastewater via heavy metals adsorption, Biomass-.-. Conv. Bioref. (2023), doi:10.1007/s13399-023-04057-4.

[7] E. Amdeha, Recovery of nanomaterials from agricultural and industrial wastes for water treatment applications, in: A.S.H. Makhlouf, G.A.M. Ali (Eds.), Waste Recycling Technologies for Nanomaterials Manufacturing, Springer International Publishing, Cham, 2021, pp. 385–417, doi:10.1007/978-3-030-68031-2_14.

[8] W.N. Wan Ismail, M.I. Arif Irwan Syah, N.H. Abd Muhet, N.H. Abu Bakar, H. Mohd Yusop, N. Abu Samah, Adsorption behavior of heavy metal ions by hybrid inulin-TEOS for water treatment, Civ. Eng. J. 8 (2022) 1787–1798, doi:10.28991/CEJ-2022-08-09-03.

[9] N. Zhu, J. Zhang, J. Tang, Y. Zhu, Y. Wu, Arsenic removal by periphytic biofilm and its application combined with biochar, Bioresour. Technol. 248 (2018) 49–55, doi:10.1016/j.biortech.2017.07.026.

[10] A. Jayakumar, C. Wurzer, S. Soldatou, C. Edwards, L.A. Lawton, O. Mašek, New directions and challenges in engineering biologically-enhanced biochar for biological water treatment, Sci. Total Environ. 796 (2021) 148977, doi:10.1016/j.scitotenv.2021.148977.

[11] X. Zhu, B. Chen, L. Zhu, B. Xing, Effects and mechanisms of biochar-microbe interactions in soil improvement and pollution remediation: a review, Environ. Pollut. 227 (2017) 98–115, doi:10.1016/j.envpol.2017.04.032.

[12] A. Sepehri, M.-H. Sarrafzadeh, Effect of nitrifiers community on fouling mitigation and nitrification efficiency in a membrane bioreactor, Chem. Eng. Process. - Process. Intensif. 128 (2018) 10–18, doi:10.1016/j.cep.2018.04.006.

[13] J. Chen, P. Zhang, J. Zhang, Y. He, Y.W. Tong, Micro–nano magnetite-loaded biochar enhances interspecies electron transfer and viability of functional microorganisms in anaerobic digestion, ACS Sustain. Chem. Eng. 10 (2022) 2811–2821, doi:10.1021/acssuschemeng.1c08288.

[14] N.M. Mubarak, J.N. Sahu, E.C. Abdullah, N.S. Jayakumar, Plam oil empty fruit bunch based magnetic biochar composite comparison for synthesis by microwave-assisted and conventional heating, J. Anal. Appl. Pyrolysis 120 (2016) 521–528, doi:10.1016/j.jaap.2016.06.026.

[15] P.R. Yaashikaa, P.S. Kumar, Fabrication and characterization of magnetic nanomaterials for the removal of toxic pollutants from water environment: a review, Chemosphere 303 (2022) 135067, doi:10.1016/j.chemosphere.2022.135067.

[16] F.S. Nworie, N. Mgbemena, A.C. Ike-Amadi, J. Ebunoha, Functionalized biochars for enhanced removal of heavy metals from aqueous solutions: mechanism and future industrial prospects, J. Hum. Earth Future 3 (2022) 377–395, doi:10.28991/HEF-2022-03-03-09.

[17] F.J. de, L. Silveira, V.C. dos Santos, J.C.S. Soares, O.C. Alves, M.I.V. Cuadros, E.M.B. Saitovitch, A.B. Gaspar, Magnetic Fe/C catalysts from coconut husk to the cyclohexene oxidation to adipic acid, J. Environ. Chem. Eng. 8 (2020) 104253, doi:10.1016/j.jece.2020.104253.

[18] F.M.T. Mendes, A.C.C. Marques, D.L. Mendonça, M.S. Oliveira, R.O. Moutta, V.S. Ferreira-Leitão, High surface area activated carbon from sugar cane straw, Waste Biomass-.-. Valoriz. 6 (2015) 433–440, doi:10.1007/s12649-015-9356-5.

[19] S.K. Lagergren, About the Theory of So-called Adsorption of Soluble Substances, Sven. Vetenskapsakad. Handingarl. 24 (1898) 1–39.

[20] G. Blanchard, M. Maunaye, G. Martin, Removal of heavy metals from waters by means of natural zeolites, Water Res. 18 (1984) 1501–1507, doi:10.1016/0043-1354(84)90124-6.

[21] I. Langmuir, The adsorption of gases on plane surfaces of glass, mica and platinum, J. Am. Chem. Soc. 40 (1918) 1361–1403, doi:10.1021/ja02242a004.

[22] H. Freundlich, Über die Adsorption in Lösungen, Z. Für Phys. Chem. 57U (1907) 385–470, doi:10.1515/zpch-1907-5723.

[23] R. Sips, On the structure of a catalyst surface, J. Chem. Phys. 16 (1948) 490, doi:10.1063/1.1746922.

[24] A.M. Puziy, O.I. Poddubnaya, A.M. Ziatdinov, On the chemical structure of phosphorus compounds in phosphoric acid-activated carbon, Appl. Surf. Sci. 252 (2006) 8036–8038, doi:10.1016/j.apsusc.2005.10.044.

[25] L.A. da Silva, S.M.S. Borges, P.N. Paulino, M.A. Fraga, S.T. de Oliva, S.G. Marchetti, M. do, C. Rangel, Methylene blue oxidation over iron oxide supported on activated carbon derived from peanut hulls, Catal. Today 289 (2016) 237–248, doi:10.1016/j.cattod.2016.11.036.

[26]

F. Wang, A novel magnetic activated carbon produced via hydrochloric acid pickling water activation for methylene blue removal, J. Porous Mater. 25 (2017) 611–619, doi:10.1007/s10934-017-0474-2.

[27] J. Yang, Y. Zhao, S. Ma, B. Zhu, J. Zhang, C. Zheng, Mercury removal by magnetic biochar derived from simultaneous activation and magnetization of sawdust, Environ. Sci. Technol. 50 (2016) 12040–12047, doi:10.1021/acs.est.6b03743.

[28] C. Chen, S. Mi, D. Lao, P. Shi, Z. Tong, Z. Li, H. Hu, Single-step synthesis of eucalyptus sawdust magnetic activated carbon and its adsorption behavior for methylene blue, RSC Adv. 9 (2019) 22248–22262, doi:10.1039/C9RA03490K.

[29] Y. Mu, H. Du, W. He, H. Ma, Functionalized mesoporous magnetic biochar for methylene blue removal: Performance assessment and mechanism exploration, Diam. Relat. Mater. 121 (2022) 108795, doi:10.1016/j.diamond.2021.108795.

[30] S. Zhang, Y. Su, S. Zhu, H. Zhang, Q. Zhang, Effects of pretreatment and FeCl3 preload of rice husk on synthesis of magnetic carbon composites by pyrolysis for supercapacitor application, J. Anal. Appl. Pyrolysis 135 (2018) 22–31, doi:10.1016/j.jaap.2018.09.026.

[31] A.L. Cazetta, O. Pezoti, K.C. Bedin, T.L. Silva, A. Paesano Junior, T. Asefa, V.C. Almeida, Magnetic activated carbon derived from biomass waste by concurrent synthesis: efficient adsorbent for toxic dyes, ACS Sustain. Chem. Eng. 4 (2016) 1058–1068, doi:10.1021/acssuschemeng.5b01141.

[32] A.-H. Lu, E.L. Salabas, F. Schüth, Magnetic nanoparticles: synthesis, protection, functionalization, and application, Angew. Chem. Int. Ed. 46 (2007) 1222–1244, doi:10.1002/anie.200602866.

[33] E.D. Revellame, D.L. Fortela, W. Sharp, R. Hernandez, M.E. Zappi, Adsorption kinetic modeling using pseudo-first order and pseudo-second order rate laws: a review, Clean. Eng. Technol. 1 (2020) 100032, doi:10.1016/j.clet.2020.100032.

[34] J. Wang, X. Guo, Adsorption kinetic models: physical meanings, applications, and solving methods, J. Hazard. Mater. 390 (2020) 122156, doi:10.1016/j.jhazmat.2020.122156.

[35] B. Arndt, K. Sellschopp, M. Creutzburg, E. Grånäs, K. Krausert, V. Vonk, S. Müller, H. Noei, G.B.V. Feldbauer, A. Stierle, Carboxylic acid induced near-surface restructuring of a magnetite surface 2019 2:1 Commun. Chem. 2 (2019) 1–8, doi:10.1038/s42004-019-0197-1.

[36] A. Drmota, A. Kosak, A. Znidarsic, A mechanism for the adsorption of carboxylic acids onto the surface of magnetic nanoparticoes, 42 (2008).

[37] J. Qu, J. Shi, Y. Wang, H. Tong, Y. Zhu, L. Xu, Y. Wang, B. Zhang, Y. Tao, X. Dai, H. Zhang, Y. Zhang, Applications of functionalized magnetic biochar in environmental remediation: a review, J. Hazard. Mater. 434 (2022) 128841, doi:10.1016/j.jhazmat.2022.128841.

[38] R. Saadi, Z. Saadi, R. Fazaeli, N.E. Fard, Monolayer and multilayer adsorption isotherm models for sorption from aqueous media, Korean J. Chem. Eng. 32 (2015) 787–799, doi:10.1007/s11814-015-0053-7.

[39] A. Gil, N. Taoufik, A.M. García, S.A. Korili, Comparative removal of emerging contaminants from aqueous solution by adsorption on an activated carbon, Environ. Technol. 40 (2019) 3017–3030, doi:10.1080/09593330.2018.1464066.

[40] Y.M. Correa-Navarro, J.C. Moreno-Piraján, L. Giraldo, Processing of fique bagasse waste into modified biochars for adsorption of caffeine and sodium diclofenac, Braz. J. Chem. Eng. 39 (2022) 933–948, doi:10.1007/s43153-021-00191-6.

[41] L.L.A. Melo, A.H. Ide, J.L.S. Duarte, C.L.P.S. Zanta, L.M.T.M. Oliveira, W.R.O. Pimentel, L. Meili, Caffeine removal using Elaeis guineensis activated carbon: adsorption and RSM studies, Environ. Sci. Pollut. Res 27 (2020) 27048–27060, doi:10.1007/s11356-020-09053-z.

[42] M. Essandoh, B. Kunwar, C.U. Pittman, D. Mohan, T. Mlsna, Sorptive removal of salicylic acid and ibuprofen from aqueous solutions using pine wood fast pyrolysis biochar, Chem. Eng. J. 265 (2015) 219–227, doi:10.1016/j.cej.2014.12.006.

[43] R. Luo, X. Li, H. Xu, Y. Sun, J. Wu, Effects of temperature, solution ph, and ball-milling modification on the adsorption of non-steroidal anti-inflammatory drugs onto biochar, Bull. Environ. Contam. Toxicol. 105 (2020) 422–427, doi:10.1007/s00128-020-02948-0.

Graphical ~~abstract~~Abstract

Images are optimised for fast web viewing. Click on the image to view the original version.

alt-text: ga1

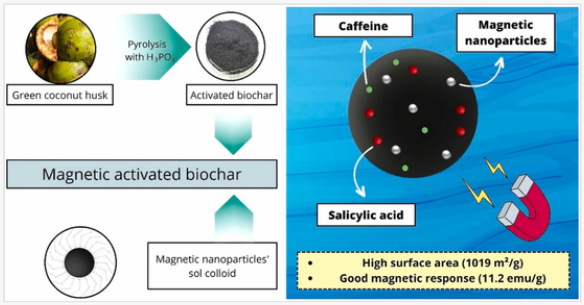

Queries and Answers

Q1

Query: Please review the **given names** (no colouring) **and surnames** (highlighted in teal colouring) to make sure that we have identified them correctly and that they are presented in the desired order. Carefully verify the spelling of all authors' names as well. If changes are needed, please provide the edits in the author section.

Answer: The given names and surnames were identified correctly

Q2

Query: Your article is being processed as a regular item to be included in a **regular issue**. Please confirm if this is correct or if your article should be published in a special issue using the responses below.

Answer: Ok. Our article should be included in a regular issue

Q3

Query: replies="Yes|No|Skip" type="boolean": Correctly acknowledging the primary **funders and grant IDs** of your research is important to ensure compliance with funder policies. Please make sure that funders are mentioned accordingly. After you have finalized your review (by accepting the current state or providing necessary changes), please click 'Reviewed' below to resolve the query.

Answer: Yes